JOM, Vol. 72, No. 5, 2020
https://doi.org/10.1007/s11837-020-04110-x




# Method for Evaluating Irradiation Effects on Flow Stress in Fe-9%Cr ODS Using TEM In Situ Cantilevers

K.H. YANO,[1,4,5] Y.Q. WU,[2,3] and J.P. WHARRY[4]

1.—Pacific Northwest National Laboratory, 622 Horn Rapids Rd, Richland, WA 99354, USA. 2.—Boise State University, 1910 University Drive, Boise, ID 83725, USA. 3.—Center for Advanced Energy Studies, 995 MK Simpson Blvd, Idaho Falls, ID 83401, USA. 4.—Purdue University, 400 Central Drive, West Lafayette, IN 47907, USA. 5.—e-mail: kayla.yano@pnnl.gov

Transmission electron microscopic (TEM) in situ mechanical testing has become a widely utilized tool for simultaneously measuring mechanical properties and understanding fundamental deformation mechanisms in irradiated and nuclear materials. Although tensile and compression specimen geometries are among the most common, opportunities remain for investigating alternative geometries that could provide unique insights into the plasticity of irradiated materials. This work demonstrates a new TEM in situ cantilever beam configuration. Cantilevers are produced from as-received and proton-irradiated (1 dpa, 500°C) Fe-9%Cr oxide dispersion-strengthened steel. Flow stress is measured using a TEM in situ depth-sensing mechanical testing holder. A 200-MPa increase in flow stress is measured due to irradiation. Size effects arise when the intrinsic (i.e., microstructural) size approaches the extrinsic (i.e., external dimensions) size and can be described using a power law relationship as a function of the material microstructure and cantilever dimensions.

## INTRODUCTION

Transmission electron microscopic (TEM) in situ mechanical testing has emerged as a key technique in evaluating nuclear materials that are volume limited due to either radioactivity associated with neutron irradiation or the shallow damage profile inherent to charged particle irradiation.[1–6] A marked advantage of TEM in situ mechanical methods is their ability to assess mechanical properties while simultaneously providing direct observation of fundamental deformation mechanisms.[7–12] However, these nanomechanical tests are strongly influenced by the specimen size effect, which arises due to the interaction between intrinsic (i.e., microstructural) and extrinsic (i.e., specimen dimensions) factors.[13–16] Specifically, elevated yield strengths are measured as specimen dimensions approach the same length scale as the microstructural obstacle spacing; this phenomenon can be expressed by a power law.[13] In more complex materials containing a denser obstacle spacing—including those obstacles created by irradiation—specimen dimensions for meaningful mechanical property testing can be as low as several hundreds of nanometers.[1,15] This allows for progressively smaller irradiated samples to be mechanically tested in situ in a TEM.

Size effects in TEM in situ mechanical tests have generally utilized compression pillars to identify a threshold at which the minimum dimension of the pillar reaches the same order as the obstacle spacing or source spacing in a material. Above this threshold, the pillars prove to be capable of meaningfully evaluating bulk-like mechanical properties, while pillars below this threshold are size-affected. Consistent threshold behaviors have been observed in compression pillars made from complex and/or irradiated materials especially relevant to the present work, including irradiated Cu,[1] Ni-base oxide dispersion-strengthened (ODS) alloy, MA6000,[17] and the same irradiated Fe-9%Cr ODS alloy studied here.[2]

Although compression pillars have been the most commonly used specimen geometries because they are relatively easy to fabricate and exhibit stress uniaxility,[18] a variety of other TEM in situ specimen configurations are becoming widely utilized for

(Published online April 1, 2020)

irradiated materials. For example, recent studies have demonstrated TEM in situ indentation,[3] tensile,[19,20] creep,[21] and bending and fracture[22] on irradiated materials. However, size effects and the threshold dimension have not been studied as extensively for other TEM in situ mechanical testing geometries beyond compression pillars. Hence, there remains a lack of understanding of how size effects may evolve in more complex materials in a variety of TEM in situ mechanical testing configurations, including cantilever bend tests.

The objective of this work is to understand size effects in the TEM in situ cantilever bend test geometry. We will focus on measuring flow stress for as-received and proton-irradiated Fe-9%Cr ODS, which is a candidate material for load-bearing components in advanced nuclear applications. Hence, its plasticity both before and after irradiation must be understood. Cantilever beams with dimensions on the order of a few 100 s of nm have been fabricated and tested in situ in a TEM. The flow stress will be described using a power law relationship as a function of the material microstructure and cantilever dimensions.

## METHODS

### Material and Irradiation

A model Fe-9%Cr ODS alloy was obtained from the Japan Nuclear Cycle Development Institute (now the Japan Atomic Energy Agency). The rod was processed by mechanically alloying ferritic steel with $Y_2O_3$ powders, then hot extruding at 1150°C. The rod was heat-treated at 1050°C for 1 h, air cooled, then tempered at 800°C, followed by a final air cool, to produce a fully martensitic grain structure. Further details regarding the fabrication of the rod and the complete composition are available in Ref. 23.

Specimens were prepared for bulk ion irradiation by electrical discharge machining of the rod into 1.5 mm × 1.5 mm × 16 mm bars. Each bar was mechanically polished through 4000 grit SiC paper, followed by electropolishing for 20 s in a 10% perchloric acid + 90% methanol solution maintained at − 40°C, with a 35-V applied potential between the specimen (anode) and platinum mesh cathode. The specimens were subsequently irradiated with 2.0 MeV protons to a fluence of $1.15 \times 10^{19}$ ions/cm$^2$ at 500°C using a 1.7-MV General Ionex Tandetron accelerator at the Michigan Ion Beam Laboratory. The beam was rastered at 2061 Hz in the vertical direction and at 255 Hz in the horizontal direction. Resistance heating and air cooling are used to maintain the irradiation temperature within ± 10°C of the target temperature, and the irradiation chamber was maintained at vacuum pressures below $1.3 \times 10^{-5}$ Pa ($10^{-7}$ Torr). The beam current was recorded throughout the duration of the experiment to ensure accurate dose accumulation. Comprehensive details on irradiation experiments are available in Ref. 24.

The displacement damage profile for 2.0-MeV protons normally incident on Fe-9%Cr was calculated using the Stopping and Range of Ions in Matter (SRIM) 2013[25] program in "Quick Calculation" (Kinchin–Pease) mode and displacements were obtained from the vacancy.txt file. The damage profile (Fig. 1) exhibits a relatively flat region between 200 nm and 10 μm, with a sharp damage peak located approximately 19 μm from the surface. All cantilever samples were taken from the depths 0.3–2.0 μm, marked "Mechanical Testing Region" in Fig. 1. In this region, the dose ranged 0.1–0.8 dpa at a dose rate of 0.4-4 × $10^{-6}$ dpa/s.

Microstructure characterization, which has already been reported in Refs. 24 and 26, was conducted at depths of 1–7 μm (also marked in Fig. 1), where the dose ranged 0.6–1.1 dpa at a dose rate of 3–5 × $10^{-6}$ dpa/s. Microstructural characterization included grain sizes, dislocation loop and line morphologies, void morphologies, carbide precipitates, and oxide nanoclusters.[24,26] All these features except for the nanoclusters were measured using an FEI (now Thermo Fisher Scientific) Tecnai TF30-FEG scanning transmission electron microscope (STEM) at the Microscopy and Characterization Suite (MaCS), Center for Advanced Energy Studies (CAES), with dislocation loops imaged using down-zone bright field STEM.[27] Oxide nanocluster morphologies and compositions were measured using atom probe tomography (APT), which enables atomic-level spatial and chemical resolution. The APT work was conducted on a CAMECA LEAP 4000× HR at MaCS, CAES. All TEM and APT imaging and operating conditions are described in greater detail in Refs. 24 and 26. This previously reported microstructure characterization was conducted at depths of 1–7 μm, corresponding to irradiation doses of 0.6–1.1 dpa. Although the

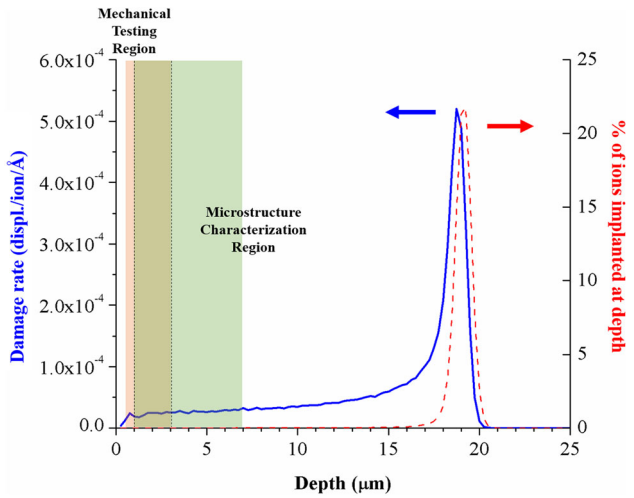


Fig. 1. Irradiation damage and ion implantation profiles for 2-MeV protons on Fe-9%Cr ODS calculated from SRIM, indicating analysis regions for mechanical testing and microstructural characterization.

cantilevers were positioned at depths of 0.3–2.0 $\mu$m, corresponding to doses of 0.1–0.8 dpa, Refs. 26, 28, and 29 suggest that the microstructure is relatively invariant between these dose ranges.

### In Situ TEM Cantilever Bend Testing

Cantilevers were prepared using an FEI Quanta 3D FEG dual-beam focused ion beam (FIB) at MaCS, CAES. A 40 $\mu$m × 15 $\mu$m × 3 $\mu$m cross-sectional lamella was lifted out from the bulk material and attached to the center post of a TEM copper half-grid, after methods initially presented in Ref. 11. The grid was held in a 45° pre-tilted stage, allowing for both perpendicular and parallel ion milling of the lamella. Up to six regions spanning 5–6 $\mu$m were designated across the lamella width, thinned to 200–350 nm, then shaped into cantilevers (Fig. 2a).

Cantilever shapes varied in length, thickness, and height (Table I). Existing stress–strain calculations exist for simple beams, where the aspect ratio (i.e., the ratio of cantilever beam length to height) is a critical parameter in determining whether a beam is simple.[30] Twenty cantilevers were made using the recommended aspect ratios ranging from 2 to 10. Based on 200- to 500-nm nominal cantilever heights, cantilever lengths were 1000, 1500, and 2000 nm. Notches were milled using the line pattern in the FIB, operating at a voltage of 10–30 keV and a current of 10 pA. Notches were nominally 100 nm long in the 500-nm height samples and 50 nm long in the 200-nm height samples. Heights and lengths were confirmed using TEM to measure the dimensions, and the thickness was measured using electron energy loss spectroscopy.

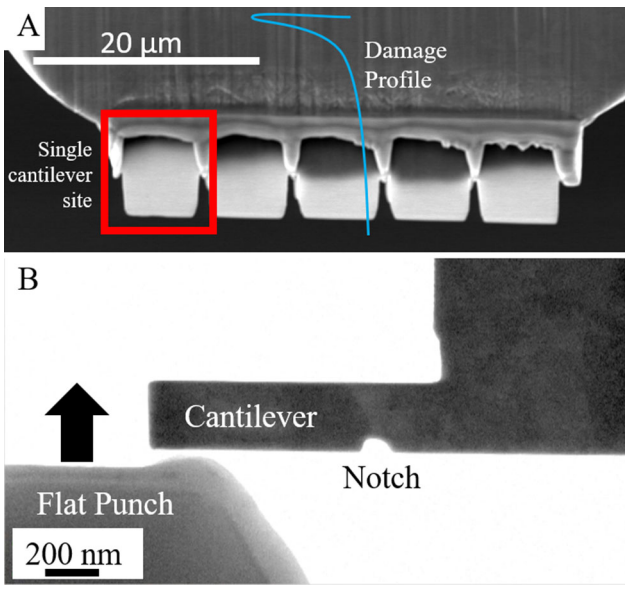


Fig. 2. Method of preparation and testing of cantilever beams; (a) five cantilever sites to be prepared after thinning, and (b) final cantilever with notch before bending, direction of loading indicated.

The in situ loading was conducted on the FEI Tecnai TF30-FEG STEM at MaCS, CAES, using a Hysitron (now Bruker) PI95 depth-sensing mechanical testing TEM holder. The holder was equipped with a flat punch tip (1 $\mu$m × 1 $\mu$m). The flat punch was aligned with the cantilever beam, and an edge of the flat punch was used to bend the free end of the cantilever. This placement of the flat punch in relation to the beam can be seen in Fig. 2b. The flat punch moves into the sample, bending the cantilever in a direction that appears oriented upward in the TEM charge-coupled device (CCD) view. Each indent was displacement-controlled to the point where the cantilevers would be bent into their base if further displacement were to occur. The displacement rates were varied to maintain a strain rate of $\approx 0.01–0.03\ s^{-1}$ at the notch, to account for varying beam lengths.[3] The Hysitron software recorded the displacement and applied load of the flat punch. The TEM CCD output is simultaneously recorded as a video file. The output is recorded at 30 frames per second and stored using MJPEG compression.

## RESULTS AND DISCUSSION

This section presents the flow stress and microstructure results sequentially, then considers the size effects in the context of the microstructure and develops power law models that are used to relate the microstructure and the mechanical properties. Videos of the as-received and irradiated cantilever beams are provided in the supplementary material.

### Flow Stress

For each cantilever, load and displacement data are collected and video is recorded of the TEM CCD screen during the bending test. With this combination of data, frame-by-frame analysis is conducted and linked to points along the load–displacement curve. Frames of a proton-irradiated cantilever with dimensions of 1500 nm long × 500 nm tall × 320 nm thick are provided in Fig. 3a–i. The accompanying load–displacement curve (adjusted for contact angle) is marked where the still frames are taken in Fig. 3j. Because this cantilever sample is $\geqq$ 200 nm thick, fine resolution of the microstructure is limited; however, there is a visible grain in the center of the beam (lighter contrast Fig. 3c). A dislocation line can be observed in Fig. 3d and e. Contour banding occurs readily and is evidenced in the quick contrast change of the center grain between Fig. 3d and e and then Fig. 3g and h. Figure 3h, f, and i shows a precipitate near the tip of the beam. Extensive plasticity occurs in the beam. With a displacement of 900 nm, the beam bends and the notch broadens, but the notch does not grow into a crack, nor does the beam fracture.

Stress–strain ($\sigma$–$\varepsilon$) curves are generated for each of the cantilevers tested using the load and

**Table I. Nominal dimensions and flow stress of all cantilevers tested; beams experiencing size effect are highlighted in italics**

| Test number | Length (nm) | Height (nm) | Thickness (nm) | Notch length (nm) | Strain, $\varepsilon$ (nm/nm) | Flow stress (MPa) |
|---|---|---|---|---|---|---|
| As-received | | | | | | |
| Test 1 | 1000 | 200 | 300 | 50 | 0.16 | 1964 |
| Test 2 | 1000 | 200 | 260 | 50 | 0.17 | 2999 |
| Test 3 | 1000 | 500 | 380 | 100 | 0.31 | 3018 |
| Test 4 | 1000 | 500 | 290 | 100 | 0.36 | 2532 |
| *Test 5* | *1500* | *200* | *320* | *50* | *0.11* | *3593* |
| *Test 6* | *1500* | *200* | *250* | *50* | *0.10* | *2637* |
| Test 7 | 1500 | 500 | 390 | 100 | 0.26 | 2297 |
| *Test 8* | *2000* | *200* | *380* | *50* | *0.08* | *4435* |
| *Test 9* | *2000* | *200* | *240* | *50* | *0.06* | *5319* |
| Test 10 | 2000 | 500 | 380 | 100 | 0.23 | 2091 |
| Average of non-size-affected | | | | | | 2634 ± 404 |
| Irradiated | | | | | | |
| Test 1 | 1000 | 200 | 350 | 50 | 0.21 | 2749 |
| Test 2 | 1000 | 200 | 270 | 50 | 0.22 | 3144 |
| Test 3 | 1000 | 500 | 380 | 100 | 0.41 | 2778 |
| Test 4 | 1000 | 500 | 290 | 100 | 0.53 | 3017 |
| *Test 5* | *1500* | *200* | *340* | *50* | *0.13* | *2690* |
| Test 6 | 1500 | 500 | 320 | 100 | 0.29 | 3080 |
| Test 7 | 1500 | 500 | 410 | 100 | 0.34 | 2022 |
| *Test 8* | *2000* | *200* | *360* | *50* | *0.10* | *4316* |
| Test 9 | 2000 | 200 | 340 | 50 | 0.18 | 2947 |
| Test 10 | 2000 | 500 | 320 | 100 | 0.18 | 2629 |
| Average of non-size-affected | | | | | | 2796 ± 335 |

displacement data collected by the Hysitron PI95, based on beam dimensions. Equations 1 and 2 are used to calculate the strain and stress, respectively, from the measured load, $L$, and displacement, $d$:

$$\varepsilon = \frac{3 * L_{\text{notch}} * t * d}{2 * L_{\text{beam}}^3} \quad (1)$$

$$\sigma = \frac{6 * L * L_{\text{notch}}}{t^2 * w} \quad (2)$$

where $L_{\text{notch}}$ is the length of the beam from the notch to the loading point, $L_{\text{beam}}$ is the entire beam length, $t$ is the beam thickness, and $w$ is the beam width. As notch lengths grow during loading, these values are updated in the calculations of stress and strain. Additionally, the stress calculation accounts for the contact angle between the cantilever and the indenter tip by adjusting the load based on the resolved force in the loading direction. It is important to note that the equations used are valid for linear–elastic problems, and that to account for plasticity, computational models would be necessary.[31] However, since such models are beyond the scope of this work, the linear–elastic equations are extended for plasticity after other micromechanical testing reports in the literature on Cu microtensile bars,[32] stress and strain calculations on Cu microcantilevers,[33] and fracture testing on NiAl microcantilevers.[34]

Representative stress–strain curves are shown for as-received and irradiated cantilevers in Fig. 4a and b, respectively. By definition, the flow stress is taken as the average stress needed to maintain plastic flow during strain hardening (i.e., between the onset of plastic yielding, up to the ultimate tensile strength).[35] However, when approaching the ultimate tensile strength, the beam has been bent to angles $> 10°$ from normal to the indenter tip. As shown in Refs. 33, 36, and 37, a high density of geometrically necessary dislocations (GNDs) is required to accommodate the large strain gradient introduced at bending angles $> 10°$. GNDs are a significant contributor to size effects in bending geometries.[38] Additionally, this $> 10°$ change in the contact angle causes considerable reductions in stress, due to the change in the normal force component of the load. So, in order to avoid both size effects and non-normal force loading, it is reasonable to limit the flow stress analysis region to the portion of strain hardening in which the bending angles are $< 10°$. The data averaged to determine flow stress are marked by a double-headed arrow in both the as-received (Fig. 4a) and proton-irradiated (Fig. 4b) conditions.

Flow stress measurements are summarized in Table I for all the as-received and proton-irradiated beams. Beam dimensions ranges are 1000–2000 nm in length, 200–500 nm in height, and 250–390 nm in thickness for both the as-received and proton-irradiated materials. Flow stress values ranges are

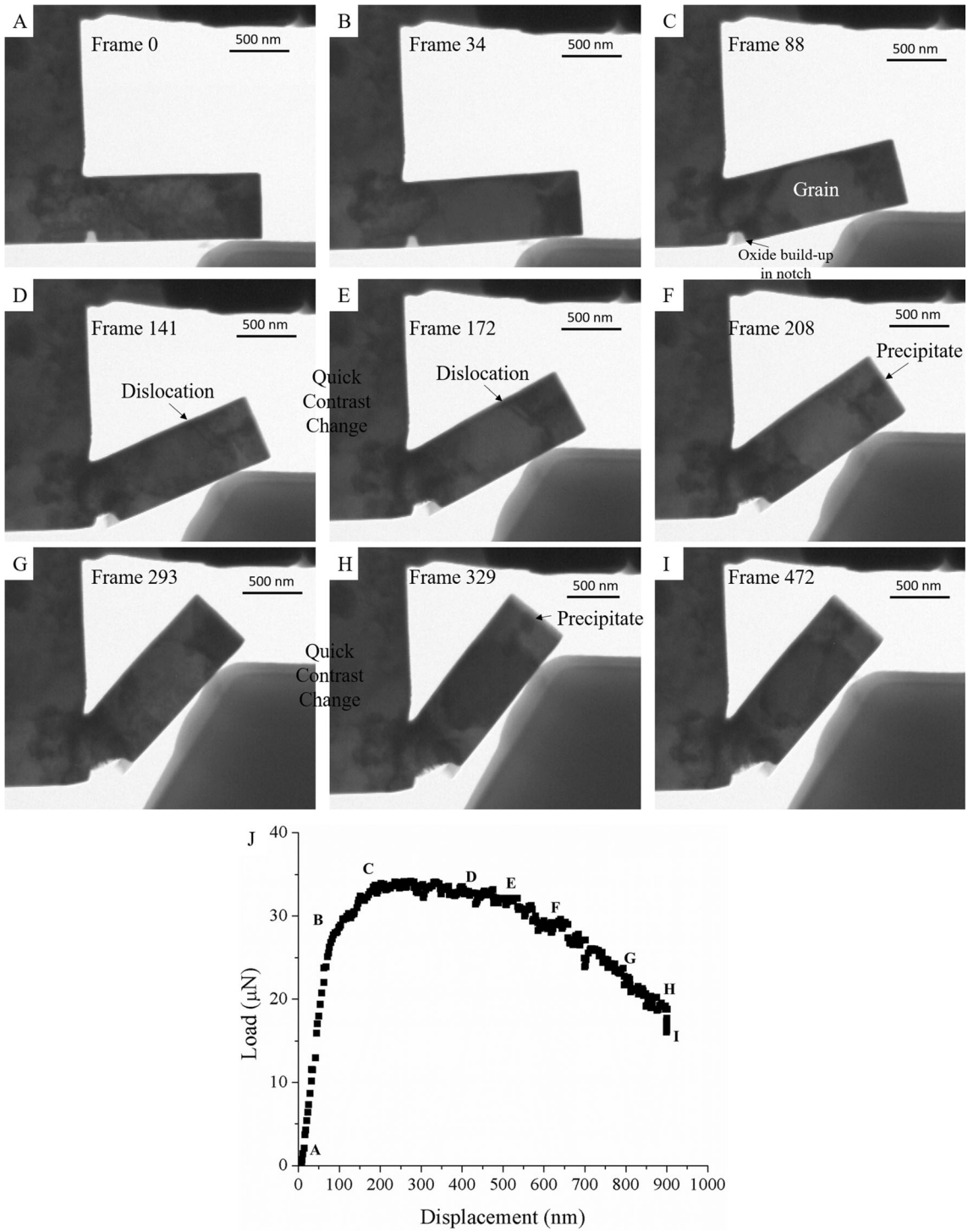


Fig. 3. Example of (a–i) still frames taken during bend test of proton irradiated cantilever, and (j) load–displacement curve (adjusted for contact angle) of tested cantilever with locations of still frames identified.

1964–5319 MPa for the as-received material and 2022–4316 MPa for the proton-irradiated material. The corresponding total strain ranges at the notch are 0.06–0.36 for the as-received cantilevers, and 0.10–0.53 for the irradiated cantilevers. Generally, samples believed to be size-affected have corresponding total strain of $< 0.15$ nm/nm and flow stress of $> 3100$ MPa (highlighted rows in Table I). However, extrinsic dimensions alone are not wholly determinative of size effects, and, as will be discussed in "Intrinsic/Extrinsic Size Effect Relationship" section, these external dimensions are normalized by microstructure to analyze size effects. The representative stress–strain curves in

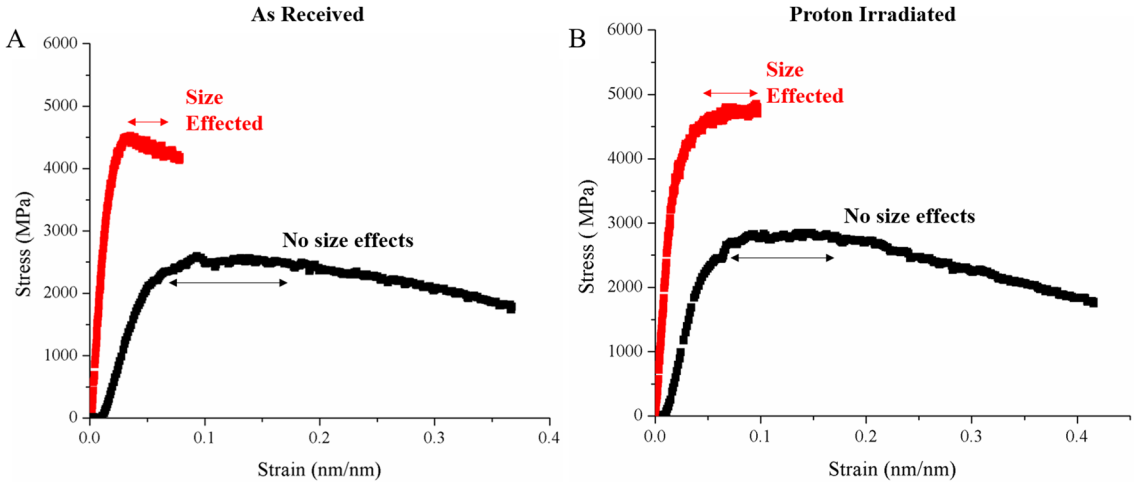


Fig. 4. Representative stress–strain curves for (a) as-received and (b) proton-irradiated cantilevers, showing both size-affected and non-size-affected results. Arrows indicate range of data used to calculate flow stress.

Fig. 4a and b also differentiate cantilevers experiencing size effects and those without size effects.

Considering only the non-size-affected samples, the average flow stress for the proton-irradiated beams is 2796 ± 335 MPa. This is nominally a 200-MPa increase over the average flow stress for the as-received beams, 2634 MPa ± 404 MPa (Table I). Yet, accounting for the error, this 200-MPa difference is negligible. The absence of hardening at irradiation temperatures of 500°C is expected from the papers by Hosemann et al. on tempered martensitic HT-9 irradiated to 2 dpa with protons at 500°C,[39] by Ando et al. on F82H with $Fe^{3+}$ at 500°C to 5 dpa,[40] and by Heintze et al. on an Fe-9Cr alloy self-ion irradiated to 1 dpa at 500°C.[41]

It is unsurprising that the cantilevers would experience extreme plasticity (as opposed to fracture) because ODS and their related bcc Fe-Cr ferritic/martensitic alloys are ductile and do not tend to exhibit intergranular fracture.[42,43] This finding is consistent with the work of Armstrong et al.[31] on self-ion-irradiated W cantilever beams tested in situ in a scanning electron microscope with beam lengths > 10 $\mu$m. In that study, W beams were unable to achieve fracture without simultaneous helium implantation, which sufficiently embrittles the material to induce intragranular fracture.[31]

## Intrinsic/Extrinsic Size Effect Relationship

For yield stress, size effects have been understood by directly relating the minimum specimen dimension to the measured yield stress. However, for flow stress, one must consider that an increasing dislocation density implies more extensive dislocation interactions during plasticity, which requires higher flow stress to sustain. This consideration manifests as a logarithmic relationship between dislocation density and flow stress, and has been observed in simulations of single crystal Ni micropillars,[44] and in experimental studies on Au nanopillars[45] and Fe pillars.[46] A model developed by Tarleton[38] formalizes this relationship for Ti and Zr cantilevers; the model relates flow stress ($\sigma_f$) with the minimum sample dimension ($w$) and the average dislocation source spacing ($w_s$) (Eq. 3). The bulk flow stress, $\sigma_0$, is the flow stress for large $w$:

$$\sigma_f = A\left(\frac{w}{w_s}\right)^{-n} + \sigma_0 \tag{3}$$

where the dislocation source density, $\rho_s$, is used to calculate the dislocation source spacing, $w_s$, according to:

$$w_s = \frac{1}{\sqrt{\rho_s}} \tag{4}$$

Because this model is based on the normalized minimum dimension (i.e., ratio of $w$–$w_s$), increasing the dislocation source density has the same effect on flow stress as decreasing the cantilever size. Hence, Tarleton's model is based on source limitation in the existing volume.

This model has been used effectively for Ti and Zr,[38] and also fits the flow stresses measured from pure Fe micropillars having an even lower source density of 1 $\mu m^{-2}$ with corresponding source spacing of 1000 nm.[46] Here, we apply the model to the Fe-9%Cr ODS cantilevers. Figure 5 shows flow stress as a function of normalized specimen dimension for both the pure Fe from Ref. 46 and the as-received and irradiated Fe-9%Cr ODS from the present study. For the pure Fe, the normalized specimen dimension is determined by taking the ratio of minimum dimension to the dislocation source spacing, which is 1000 nm. However, for the Fe-9%Cr ODS, the total obstacle spacing is utilized instead of the dislocation source spacing.

The obstacle spacing is determined from microstructure characterization of the as-received and irradiated materials, and is primarily adopted

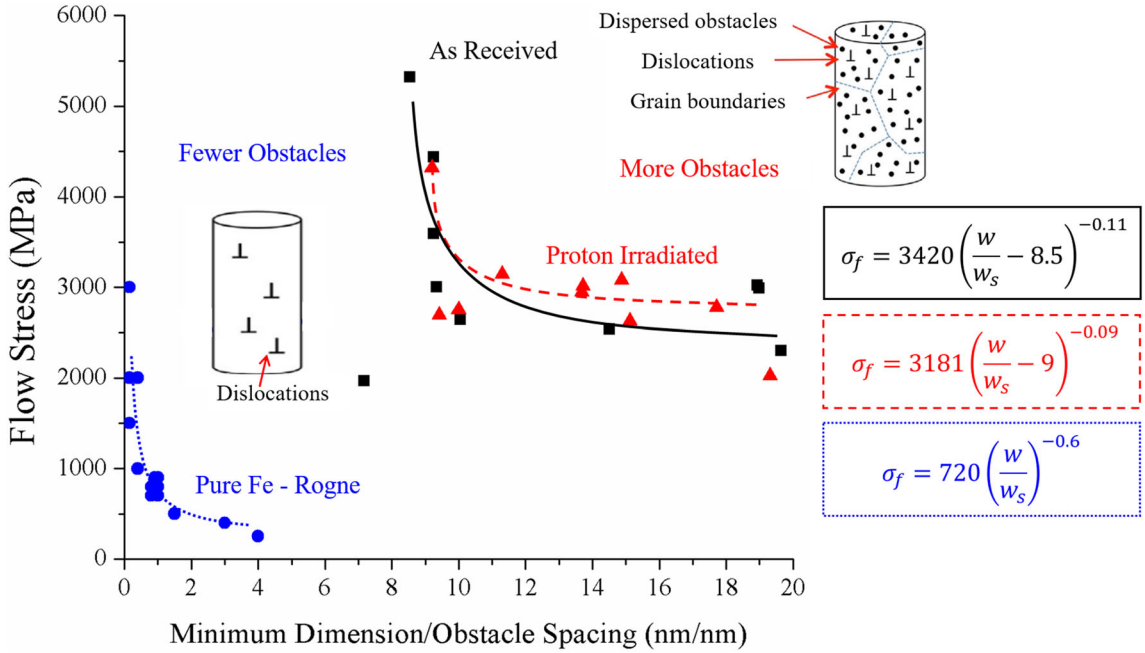


Fig. 5. Decaying exponential relationship between the flow stress and normalized minimum specimen dimension for as-received and irradiated ODS (black squares, red triangles) and pure Fe (blue circles) cantilevers. Shift between pure Fe and ODS to higher normalized minimum dimensions is attributed to microstructure (inset cartoons) (Color figure online).

from Swenson and Wharry.[24,26] Unirradiated Fe-9%Cr ODS consists of dense dislocation regions, a fine dispersion of oxide nanoclusters, and 200- to 300-nm-diameter grains. After irradiation, voids and dislocation loops nucleate at number densities of $0.34 \times 10^{21}$ m$^{-3}$ and $10.2 \times 10^{21}$ m$^{-3}$, with diameters of 4 nm and 8.4 nm, respectively. Grain diameter and dislocation line density remain statistically unchanged with irradiation, at 230–310 nm and 17.6-19.1 $\times 10^{14}$ m$^{-2}$, respectively. Nanocluster diameter reduces (from 5.96 nm to 4.77 nm), while their overall number density remains constant ($560 \times 10^{21}$ as compared to $568 \times 10^{21}$ m$^{-3}$). The microstructure quantification from Ref. 24 for both the as-received and proton-irradiated conditions are summarized in Table II. Considering all these microstructural features, the obstacle spacing is calculated for both the as-received and irradiated ODS through a diameter-weighted number density approach, as outlined in Ref. 47. There is little difference in obstacle spacing between the as-received and proton-irradiated conditions: 19.9 nm as compared to 21.2 nm. This calculated obstacle spacing is also included in Table II for easy comparison.

The as-received and irradiated ODS both exhibit the expected decaying exponential relationship between the flow stress and the normalized minimum dimension (Fig. 5). These trends reveal that elevated flow stress values occur at normalized dimensions $< 9$ nm/nm for the Fe-9%Cr ODS, whereas the flow stress reaches a constant value of $\sim 3000$ MPa at normalized dimensions $> 9$ nm/nm. The Fe-9%Cr ODS flow stress results are consistent with the specimen size effect as reported for yield strength,[36,48,49] while the normalization of the minimum dimension to the microstructure highlights the role of source or obstacle spacing within an existing specimen volume.

The power law can be fitted to the flow stresses of the as-received and proton-irradiated ODS, but an additional factor, $B$, is necessary for the fit:

$$\sigma_f = A\left(\frac{w}{w_s} - B\right)^{-n} \tag{5}$$

where $A$ and $n$ are the stress proportionality constant and stress exponent, respectively. A notable limitation of the power law is its asymptotic approach to infinite flow stress at the limit of the ratio $w/w_s$. However, for the purposes here, the power law is used only for understanding relative behaviors between datasets, and not as a rigorous physical representation of deformation mechanisms. In the following paragraphs, each of the three key variables ($A$, $n$, $B$) is determined for the experiments performed here, and their meaning and implications on plasticity are subsequently discussed. The values of each variable used to fit the ODS and pure Fe data are shown in the equations overlaid in Fig. 5.

*Stress proportionality constant* The stress proportionality constant, $A$, for the as-received and proton-irradiated ODS are 3420 and 3181, respectively. In comparison, the pure Fe has a stress proportionality constant of 720. This constant is tied to the bulk flow stress. The difference between the ODS and the pure Fe can be primarily understood through the

**Table II. Microstructure of as-received and proton-irradiated Fe-9%Cr ODS, summarized from Ref. 24, with calculated obstacle spacing on the glide plane**

| Feature | Measurement | As-received | Proton-irradiated (3 dpa, 500°C) |
|---|---|---|---|
| Grains/laths | # of grains measured | 104 | 104 |
| | Effective diameter ($\times 10^{-6}$ m) | 0.23 ± 0.12 | 0.31 ± 0.11 |
| Dislocation lines | # of measurements | 17 | 46 |
| | Density ($\times 10^{14}$ m$^{-2}$) | 19.1 ± 3.8 | 17.6 ± 5.3 |
| | Obstacle spacing (nm) | 22.8 | 23.8 |
| Carbide precipitates | # of carbides measured | 36 | 51 |
| | Effective diameter ($\times 10^{-6}$ m) | 0.11 ± 0.07 | 0.07 ± 0.03 |
| | Density ($\times 10^{20}$ m$^{-3}$) | 0.20 | 0.46 |
| | Obstacle spacing (nm) | 670 | 560 |
| Voids | # of voids measured | 0 | 8 |
| | Diameter ($\times 10^{-9}$ m) | – | 4.00 ± 1.51 |
| | Density ($\times 10^{21}$ m$^{-3}$) | – | 0.34 ± 0.44 |
| | Obstacle spacing (nm) | – | 860 |
| Dislocation loops | # of loops measured | 0 | 688 |
| | Diameter ($\times 10^{-9}$ m) | – | 8.4 ± 1.7 |
| | Density ($\times 10^{21}$ m$^{-3}$) | – | 10.2 ± 8.0 |
| | Obstacle spacing (nm) | – | 108 |
| Oxide nanoclusters | # of clusters measured | 486 | 964 |
| | Average diameter (nm) | 5.96 ± 0.14 | 4.77 ± 0.06 |
| | Density ($\times 10^{21}$ m$^{-3}$) | 568 | 560 |
| | Obstacle spacing (nm) | 17.2 | 19.3 |
| Average obstacle spacing on glide plane (nm) | | 19.9 | 21.2 |

addition of solid solution strengthening and oxide dispersion strengthening to the ODS.[35,50] Hence a larger flow stress is required to continually plastically deform the ODS than the pure Fe.

*Stress exponent* The stress exponent, $n$, has values of 0.11 and 0.09 for the as-received and proton-irradiated ODS, respectively. Direct empirical measurements in the literature show $n$ varying from 0.2 to 0.5 for bcc metals, depending on orientation and loading conditions,[51] which is notably higher than the values determined here. However, Dunstan and Bushby[52] argue that the stress exponent is an arbitrary value, controlled by the sample dimension and the flow strain, rather than by any fundamental mechanism. Rather than compare stress exponents across experiments in the archival literature, they suggest relating the sample dimensions ($w$) and flow strain ($c$) from the experimental conditions to calculate an expected stress exponent range:

$$n = \frac{1.5/w}{c + 1.5/w} \tag{6}$$

In this study, the flow strain measured at the notch varies from 0.06 to 0.53 for both the as-received and proton-irradiated cantilevers. Using the minimum and maximum values for beam heights of 140 and 515 nm for $w$, Eq. 6 predicts a stress exponent range of 0.01–0.15, which is consistent with the $n$ values fitted to our empirical data in Fig. 5. Carrying out the same calculation on Rogne's pure Fe data, stress exponent values are predicted to be in the range 0.5–0.6, again consistent with the fit.

*Offset factor* The pure Fe and ODS exhibit the most notable difference in behavior when considering the offset factor, $B$. Specifically, $B$ can be taken to be 0 in pure Fe (i.e., per Eq. 3), 8.5 nm/nm for the as-received ODS, and 9 nm/nm for the proton-irradiated ODS. These differences in $B$ values are likely attributed to differences in deformation mechanisms between pure Fe and ODS, which are associated with the influence of the varying obstacle and source spacings on the dislocation motion. For instance, pure Fe has a low dislocation source density (i.e., high dislocation source spacing), and dislocation–dislocation interaction is minimal. The grain size is such that Rogne's pillars[46] are often fully contained within a single grain. The material plasticity is limited by dislocation glide on available slip planes without grain boundary interactions or constraints from neighboring grains.[35] In contrast, the Fe-9%Cr ODS has a considerably lower obstacle spacing than pure Fe; as such, dislocation–dislocation interactions as well as dislocation interactions with oxide nanoclusters and irradiation-induced dislocation loops and voids are plentiful. In the Fe-9%Cr ODS microstructure, dislocations must bow around obstacles and/or cross-slip in order for

plasticity (i.e., flow) to continue, and the plastic zone is increasingly confined. Further, since the ODS grain size is on the order of 200–300 nm, the cantilever beams can contain multiple grains. This suggests that the resolved shear stress and dislocation mobility at the notch could be affected by adjacent grains having high Schmid or Taylor factors. This argument can be visualized by considering a fixed nano/microscale specimen volume but containing low ($B \sim 0$–1) or high ($B > 8$) source/obstacle spacing; the reader is referred to the cartoons overlaid on Fig. 5 for a pictorial representation. The offset factor $B$ must be considered in flow stress testing of more complex materials to account for the increased complexity of dislocation slip, constraints, and the associated consequences of these complexities on the deformation mechanisms.

Because of their differences in $B$ values, the size effect threshold occurs at a larger normalized minimum dimension for the ODS than for pure Fe. This normalized minimum dimension is essentially the slope of a line on a plot of the minimum allowable specimen dimension (i.e., extrinsic size) versus obstacle spacing (i.e., internal microstructural size), as can be seen in Fig. 4 in Ref. 15. As obstacle spacing is reduced, the allowable minimum dimension to avoid size effects also reduces; likewise, as obstacle spacing increases (towards perfect crystallinity), the minimum allowable dimension becomes increasingly large. This is consistent with observations in the archival literature that suggest that progressively smaller specimen geometries can be used to obtain meaningful mechanical properties in materials having increased obstacle densities.[1,15,17,36,46,52–57] This observation corroborates the idea that the shift in $B$ from 0 to $\sim 9$ with increasing material complexity is due to fundamental differences in deformation mechanisms inherent to more complex materials. These complexities are not fully captured with the parameters of Eq. 3 (original power law), thus requiring the offset factor $B$ to fit the size effect power law for more complex materials, i.e., Equation 6. Consequently, the non-normalized minimum dimension for meaningful flow stress measurements in Fe-9%Cr ODS is 180–190 nm, whereas that for pure Fe is a factor of five larger.

## CONCLUSION

Nanoscopic notched cantilever beams were made from as-received and irradiated (2 MeV protons, 500°C, 3 dpa) Fe-9%Cr ODS and loaded in situ in a TEM. Load–displacement data were collected and flow stress was calculated. Major conclusions are as follows:

1) Flow stress is related to cantilever dimensions and microstructure according to a power law relationship. Stress exponents are fit to a power law and are consistent with exponential values calculated based on the given specimen dimension and flow strain.
2) For Fe-9%Cr ODS, the minimum allowable dimension of the cantilever geometry to measure flow stress without size effects is 180–190 nm, a factor of five times smaller than that of pure Fe. This is due to differences in deformation mechanisms, complex dislocation interactions, and plastic zone confinement in increasingly complex materials. Consequently, an offset factor, B, must be included in the power law fit.
3) Flow stress is calculated from the cantilevers for Fe-9%Cr ODS. None of the beams fractured. While the cantilever geometry is relatively simple to prepare by FIB milling, the complexity introduced with this geometry presents an added challenge to extract stress, strain, and strain-hardening exponents, in comparison with microcompression pillars or microtensile samples.

## ACKNOWLEDGEMENTS

This research was sponsored in part by the National Science Foundation CAREER award DMR-17-52636 (JPW), and the US DOE Office of Nuclear Energy project DE-NE0008758 (KHY). Microscopy work was supported by the US DOE Nuclear Science User Facilities experiments 15-540, 16-656, and 18-1168. The authors thank J. Burns and J. Taylor in the Microscopy and Characterization Suite (MaCS) at CAES for their assistance with FIB and TEM, J. Noble from Bruker with the setup and operation of the PI95, and Matthew Swenson at the University of Idaho for many thought-provoking technical discussions. The authors also acknowledge the staff and students at the Michigan Ion Beam Laboratory for their assistance with ion irradiation.

## ELECTRONIC SUPPLEMENTARY MATERIAL

The online version of this article (https://doi.org/10.1007/s11837-020-04110-x) contains supplementary material, which is available to authorized users.

## REFERENCES

1. D. Kiener, P. Hosemann, S.A. Maloy, and A.M. Minor, *Nat. Mater.* 10, 608 (2011).
2. K.H. Yano, M.J. Swenson, Y. Wu, and J.P. Wharry, *J. Nucl. Mater.* 483, 107 (2017).
3. K.H. Yano, S. Thomas, M.J. Swenson, Y. Lu, and J.P. Wharry, *J. Nucl. Mater.* 502, 201 (2018).
4. H.J. Qu, K.H. Yano, P.V. Patki, M.J. Swenson, and J.P. Wharry, *J. Mater. Res.* 1 (2019).
5. G.S. Jawaharram, P.M. Price, C.M. Barr, K. Hattar, R.S. Averback, and S.J. Dillon, *Scr. Mater.* 148, 1 (2018).
6. S. Mao, S. Özerinç, W.P. King, R.S. Averback, and S.J. Dillon, *Scr. Mater.* 90, 29 (2014).

7. M. Jin, A.M. Minor, E.A. Stach, and J.W. Morris, *Acta Mater.* 52, 5381 (2004).
8. Q. Yu, R.K. Mishra, and A.M. Minor, *JOM* 64, 1235 (2012).
9. J.T.M. De Hosson, *Microsc. Res. Tech.* 72, 250 (2009).
10. X.L. Wu, Y.Z. Guo, Q. Wei, and W.H. Wang, *Acta Mater.* 57, 3562 (2009).
11. P.J. Imrich, C. Kirchlechner, D. Kiener, and G. Dehm, *JOM* 67, 1704 (2015).
12. Z. Shan, *JOM* 64, 1229 (2012).
13. J.R. Greer and J.T.M. De Hosson, *Prog. Mater Sci.* 56, 654 (2011).
14. E. Arzt, *Acta Mater.* 46, 5611 (1998).
15. J.P. Wharry, K.H. Yano, and P.V. Patki, *Scr. Mater.* 162, 63 (2019).
16. G. Dehm, B.N. Jaya, R. Raghavan, and C. Kirchlechner, *Acta Mater.* 142, 248 (2017).
17. B. Girault, A.S. Schneider, C.P. Prick, and E. Arzt, *Adv. Eng. Mater.* 12, 385 (2010).
18. P. Hosemann, C. Shin, and D. Kiener, *J. Mater. Res.* 30, 1231 (2015).
19. C. Chisholm, *Quantitative In Situ TEM Studies of Small-Scale Plasticity in Irradiated and Unirradiated Metals* (Berkeley: University of California, 2015).
20. M.S. Ding, L. Tian, W.Z. Han, J. Li, E. Ma, and Z.W. Shan, *Phys. Rev. Lett.* 117, 1 (2016).
21. D.C. Bufford, C.M. Barr, B. Wang, K. Hattar, and A. Haque, *JOM* 71, 3350 (2019).
22. W.Z. Han, M.S. Ding, and Z.W. Shan, *Scr. Mater.* 147, 1 (2018).
23. S. Ohtsuka, S. Ukai, M. Fujiwara, T. Kaito, and T. Narita, *Mater. Trans.* 46, 487 (2005).
24. M.J. Swenson and J.P. Wharry, *J. Nucl. Mater.* 467, 97 (2015).
25. J.F. Ziegler, *Stopping Range of Ions in Matter* (2013).
26. M.J. Swenson and J.P. Wharry, *J. Nucl. Mater.* 496, 24 (2017).
27. C.M. Parish, K.G. Field, A.G. Certain, and J.P. Wharry, *J. Mater. Res.* 30, 1275 (2015).
28. S.J. Zinkle and L.L. Snead, *Scr. Mater.* 143, 154 (2018).
29. R.D. Carter, D.L. Damcott, M. Atzmon, G.S. Was, and E.A. Kenik, *J. Nucl. Mater.* 205, 361 (1993).
30. D.E.J. Armstrong, A.J. Wilkinson, and S.G. Roberts, *J. Mater. Res.* 24, 3268 (2009).
31. D.E.J. Armstrong, C.D. Hardie, J.S.K.L. Gibson, A.J. Bushby, P.D. Edmondson, and S.G. Roberts, *J. Nucl. Mater.* 462, 374 (2015).
32. D. Kiener, P. Kaufmann, and A.M. Minor, *Adv. Eng. Mater.* 14, 960 (2012).
33. M.W. Kapp, C. Kirchlechner, R. Pippan, and G. Dehm, *J. Mater. Res.* 30, 791 (2015).
34. F. Iqbal, J. Ast, M. Göken, and K. Durst, *Acta Mater.* 60, 1193 (2012).
35. M. Meyers and K. Chawla, *Mechanical Behavior of Materials* (New York: Cambridge University Press, 2009).
36. C. Motz, T. Schöberl, and R. Pippan, *Acta Mater.* 53, 4269 (2005).
37. J. Gong and A.J. Wilkinson, *Acta Mater.* 57, 5693 (2009).
38. E. Tarleton, D.S. Balint, J. Gong, and A.J. Wilkinson, *Acta Mater.* 88, 271 (2015).
39. P. Hosemann, C. Vieh, R.R. Greco, S. Kabra, J.A. Valdez, M.J. Cappiello, and S.A. Maloy, *J. Nucl. Mater.* 389, 239 (2009).
40. M. Ando, H. Tanigawa, S. Jitsukawa, T. Sawai, Y. Katoh, A. Kohyama, K. Nakamura, and H. Takeuchi, *J. Nucl. Mater.* 307–311, 260 (2002).
41. C. Heintze, F. Bergner, and M. Hernández-Mayoral, *J. Nucl. Mater.* 417, 980 (2011).
42. R.L. Klueh and D.R. Harries, *High-Chromium Ferritic and Martensitic Steels for Nuclear Applications* (AsTM: West Conshohocken, 2001).
43. A. Chauhan, J. Hoffman, D. Litvinov, and J. Aktaa, *Mater. Sci. Eng. A* 707, 207 (2017).
44. H. Tang, K.W. Schwarz, and H.D. Espinosa, *Acta Mater.* 55, 1607 (2007).
45. S.W. Lee, S.M. Han, and W.D. Nix, *Acta Mater.* 57, 4404 (2009).
46. B.R.S. Rogne and C. Thaulow, *Philos. Mag.* 95, 1814 (2015).
47. M.J. Swenson, C.K. Dolph, and J.P. Wharry, *J. Nucl. Mater.* 479, 426 (2016).
48. W.D. Nix and H.J. Gao, *J. Mech. Phys. Solids* 46, 411 (1998).
49. M.D. Uchic, D.M. Dimiduk, J.N. Florando, and W.D. Nix, *Science* 305, 986 (2004).
50. W.D.J. Callister and D.G. Rethswich, *Materials Science and Engineering*, 9th ed. (Hoboken: Wiley, 2014).
51. A.S. Schneider, B.G. Clark, C.P. Frick, P.A. Gruber, and E. Arzt, *Mater. Sci. Eng. A* 508, 241 (2009).
52. D.J. Dunstan and A.J. Bushby, *Int. J. Plast.* 40, 152 (2013).
53. B. Ehrler, X.D. Hou, T.T. Zhu, K.M.Y. P'Ng, C.J. Walker, A.J. Bushby, and D.J. Dunstan, *Philos. Mag.* 88, 3043 (2008).
54. R. Soler, J.M. Wheeler, H.J. Chang, J. Segurado, J. Michler, J. Llorca, and J.M. Molina-Aldareguia, *Acta Mater.* 81, 50 (2014).
55. C.P. Frick, B.G. Clark, S. Orso, A.S. Schneider, and E. Arzt, *Mater. Sci. Eng. A* 489, 319 (2008).
56. D.M. Dimiduk, M.D. Uchic, and T.A. Parthasarathy, *Acta Mater.* 53, 4065 (2005).
57. P.V. Patki, *Microstructure Evolution and TEM In Situ Mechanical Testing of Proton Irradiated Nanocrystalline Copper Tantalum Alloy* (West Lafayette: Purdue University, 2018).